Numerical Simulation of Micro and Nano Scale Fracture

M. Zhou

The George W. Woodruff School of Mechanical Engineering
Georgia Institute of Technology
Atlanta, GA 30332-0405, U.S.A.
(404) 894-3294, (404) 894-0186 (Fax)
min.zhou@me.gatech.edu

ABSTRACT

Damage and fracture in a titanium diboride/alumina (TiB_2/Al_2O_3) ceramic composite system is analyzed numerically. The materials have two-phase microstructures with various phase distributions. The simulations concern the effects of interfacial bonding strength and phase morphologies on damage and fracture development. A micromechanical model that provides explicit account for arbitrary microstructures and arbitrary damage and fracture patterns is developed and used. The approach uses both a constitutive law for the bulk solid constituents and a constitutive law for fracture surfaces. The interfacial relation allows the energy dissipation during fracture processes to be tracked. When assessed as a fraction of the cohesive energy for the undamaged interfaces, this irreversible energy loss can be used as a measure for damage associated with crack and microcrack development. The cohesive finite element model also allows fracture to evolve as an outcome of bulk material response, interfacial behavior and applied loading. Calculations show that the failure mode is significantly influenced by the interfacial bonding strength between the phases. When weak interfacial bonding exists, microcrack initiation and growth are the principal mode of failure. Whereas when strong interfacial bonding is derived from material processing, the extension of a dominant crack is observed.

KEY WORDS

Ceramic composites, fracture, cohesive finite element modeling

INTRODUCTION

An important issue for ceramic materials in applications is their failure resistance, including strength and fracture toughness, Komanduri (1989) [1] and Messer (1995) [2]. The fracture toughness of these materials is at least an order of magnitude lower than those of metals and polymers. Progress has been made in developing advanced ceramic materials using the fact that the materials derive significantly higher toughness from microscopic or nanosized reinforcements. For example, Niihara et al. (1993) [3] reported that a 5% population of SiC nanoparticles increases the tensile strength of Si_3N_4 from 350 MPa to 1 GPa and improves its fracture toughness from 3.25 to 4.7 $\mathrm{MPa}\sqrt{\mathrm{m}}$. Alumina/titanium diboride (Al_2O_3/TiB_2) composites with a wide range of microstructural phase sizes and morphologies have been developed, Logan (1992, 1996) [4-5]. The different microstructures are derived from a range of processing conditions through self-propagating high temperature synthesis or mixing of constituent powders followed by hot pressing. These materials have shown fracture toughness values between 3.5 and 4.9 $\mathrm{MPa}\sqrt{\mathrm{m}}$. These results suggest it is possible to further enhance

properties through microstructural engineering. Potential applications of these materials include cutting tool inserts, electrodes and ceramic armor. Although microstructure-induced, size-dependent toughening mechanisms at the micro and nano levels are demonstrated approaches for property enhancement, the physics for such effects has not been well quantified. In order to develop more advanced materials, it is necessary to characterize the influences of phase morphology, phase length scale, and interfacial bonding on fracture toughness.

Despite the success of continuum damage mechanics and fracture mechanics on the macroscopic level, damage and failure on microscopic levels are far from being well-characterized due to microstructural complexities and size-dependent deformation mechanisms. Most available models for the failure are, for the most part, continuum damage theories in which the net effect of fracture is idealized as a degradation of the elasticity modulus, see e.g. Curran et al. (1993) [6], Rajendran (1994) [7], Johnson and Holmquist (1992) [8], Espinosa et al. (1995) [9]. While capturing the macroscopic or effective response, these models do not explicitly consider the discrete nature of fracture through crack growth and coalescence. Thus, they lack the ability to account for the interaction among cracks. In addition, the effect of microstructural entities such as inclusions, fibers and grains on crack path and fracture toughness can not be explicitly analyzed. The lack of models that provide *explicit* account for arbitrary microstructural morphologies *and* microscopic fracture patterns makes it difficult to identify and design microstructural configurations which enhance fracture toughness. The nonexistence of analytical tools also poses a challenge to explicating size-induced toughening mechanisms which significantly influence the behavior of micro and nanostructured materials.

Explicit micromechanical modeling and simulation represent a unique means for analyzing nano and micro toughening mechanisms and for elucidating scaling laws. Through the consideration of actual microstructures, the effects of various fracture mechanisms can be delineated. A micromechanical cohesive finite element method (CFEM) for *explicit* fracture analysis has been developed recently, Zhai and Zhou (1999) [10]. Based on a cohesive surface formulation of Xu and Needleman (1994) [11], this approach allows explicit modeling and simulation of fracture over a range of length scales, providing a much-needed tool for studying microstructure-induced toughening in heterogeneous materials. The unique advantages of the CFEM include (1) it allows explicit account of real, arbitrary material microstructures, (2) it permits explicit modeling of fracture in a non-constrained manner therefore arbitrary crack paths or microcrack patterns are admitted, and (3) it is capable of resolving fracture explicitly over multiple length scales and is free of the limitations of any *ad hoc* fracture criteria applicable over only a certain range of sizes (e.g. continuum criteria which assume the existence of K-fields). The obviation of fracture criteria assigns a predictive power to models using this approach. Consequently, crack initiation, crack growth, crack path, crack or microcrack patterns, and crack speed evolve as natural outcomes of material response, applied loading, and boundary constraint.

The effects of microstructural morphologies on fracture resistance and the effect of interphase bonding strength on fracture mode have been analyzed by Zhai and Zhou (1998, 1999) [12, 10]. The analysis reported here concerns primarily the characterization of damage and the effect of interfacial bonding strength on damage distribution.

PROBLEM FORMULATION

To account for the finite strains involved in crack tip regions, a finite deformation formulation is used. The independent variables are the position of a material point in the reference configuration $\mathbf{x}$, and time t. Relative to a fixed Cartesian frame $\{\xi^i\}$, a material point initially at x occupies position $\bar{\mathbf{x}}$ in the current configuration. The displacement vector and the deformation gradient are defined as $\mathbf{u} = \bar{\mathbf{x}} - \mathbf{x}$ and $\mathbf{F} = \partial\bar{\mathbf{x}}/\partial\mathbf{x}$, respectively. The principle of virtual work includes a contribution from the cohesive surfaces and is written as

$$\int_V \mathbf{s} : \delta\mathbf{F} dV - \int_{S_{\text{int}}} \mathbf{T} \cdot \delta\boldsymbol{\Delta} dS = \int_{S_{ext}} \mathbf{T} \cdot \delta\mathbf{u} dS - \int_V \rho \frac{\partial^2 \mathbf{u}}{\partial t^2} \cdot \delta\mathbf{u} dV, \tag{1}$$

where $\mathbf{s}:\delta\mathbf{F} = s^{ij}\delta F_{ji}$, s is the nonsymmetric first Piola-Kirchhoff stress; $\mathbf{\Delta}$ is the displacement jump across a pair of cohesive surfaces; V, S_{ext} and S_{int} are the volume, external surface area and internal cohesive surface area, respectively, of the body in the reference configuration. The density of the material in the reference configuration is ρ. Also, $\delta\mathbf{F}, \delta\mathbf{\Delta}$, and $\delta\mathbf{u}$ denote admissible variations in F, $\mathbf{\Delta}$ and u respectively. The traction vector $\mathbf{T}$ and the surface normal in the reference configuration $\mathbf{n}$ are related through $\mathbf{T} = \mathbf{n}\cdot\mathbf{s}$. The volumetric constitutive law is hyperelastic, Xu and Needleman (1994) [11].

The constitutive law for cohesive surfaces relates the traction and displacement jumps across crack surfaces. In this formulation, an equivalent separation $\Delta = \sqrt{\Delta_n^2 + \alpha^2\Delta_t^2}$ and an equivalent traction $\overline{T} = \sqrt{T_n^{\,2} + T_t^{\,2}}$ are defined, where Δ_n and Δ_t denote the normal and tangential components of the relative displacement across a cohesive surface pair, T_n and T_t are normal and shear traction components, and $\alpha = \Delta_{nc}/\Delta_{tc}$ with Δ_{nc} and Δ_{tc} the corresponding critical normal and tangential separations at which cohesive stresses T_n and T_t vanish under pure mode I and mode II conditions, respectively. The cohesive relation is specified between $\overline{T}$ and Δ. A bilinear cohesive law is used, as illustrated in Fig. 1. The normal and tangential traction components are, respectively

$$\left.\begin{aligned} T_n &= \frac{\overline{T}(\Delta)}{\Delta}\Delta_n \\ T_t &= \frac{\overline{T}(\Delta)}{\Delta}\Delta_t \end{aligned}\right\}, \tag{2}$$

where

$$\overline{T}(\Delta) = \begin{cases} T_{max}\dfrac{\Delta}{\eta\Delta_c}, & \text{for } \Delta \le \eta\Delta_c; \\ \overline{T}(\Delta) = T_{max} - \dfrac{\Delta}{\Delta_c}, & \text{for } \Delta \ge \eta\Delta_c. \end{cases} \tag{3}$$

In the above expressions, Δ_c is the critical separation at which cohesive traction $\overline{T}$ vanishes and $0 < \eta < 1$ is a parameter specifying the separation ($\eta\Delta_c$) at which maximum traction T_{max} occurs. Loading and unloading follow the arrows in Fig. 1. During the stage of rising traction (A-B), the separation process is elastic and cohesive energy accumulated is recoverable. During the descending part of the traction-separation relation (B-C), damage is assumed to occur and unloading follows path P-A. The cohesive energy ϕ_0 is the amount of energy required to generate a unit crack surface area. It is a measure of the energy consumption during fracture. The above bilinear relation implies the partition of ϕ_0 into a recoverable part ϕ_r and an irreversible part ϕ_d. The irreversible part ϕ_d is partly converted into surface energy of crack surfaces and partly spent on causing damage in the material adjacent to crack surfaces through microcrack formation not explicitly modeled. Apparently, $\phi_d(\Delta)$ increases with Δ and when full separation is achieved, $\phi_d(\Delta_c) = \phi_0$. Consequently,

$$D = \frac{\phi_d}{\phi_0} \tag{4}$$

can be used a relatively measure for damage. Note that $0 \le D \le 1$, with $D = 0$ indicating fully recoverable interfacial separation and $D = 1$ signifying complete separation or total fracture. In the following analysis, D will be used as an internal state variable quantifying the degree of the damage, providing a phenomenological measure for failure analysis. The spatial and time variation of $D = D(\mathbf{x},t)$ allows the distribution and evolution of damage in various microstructures to be analyzed.

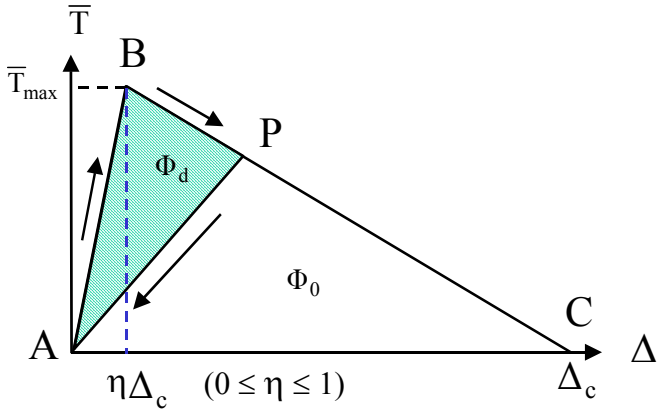

Fig. 1 Cohesive Separation Law

Computations are carried out for a center-cracked specimen. The specimen has an initial height of $2H = 1.6\,\text{mm}$ and an initial width of $2L = 1.6\,\text{mm}$. An initial crack of length $2a_i = 0.4\,\text{mm}$ exists along the ξ^1 axis. Only one half of the specimen $(\xi^1 > 0)$ is discretized and modeled in the simulations because of the symmetry with respect to the ξ^2 axis. Conditions of plain strain are assumed to prevail. The small region in front of the crack tip contains microstructures digitized from micrographs of actual composite materials. Inside this region, the material inhomogeneities and material phase distribution are explicitly modeled. In the microstructure analyzed here, TiB_2 particles are embedded in the alumna matrix. The average particle size is approximately 10-20 μm. The bulk properties of each finite element are those for either the particles or those for the matrix. The properties of each segment of potential fracture surface are specified according to its location as those belonging to the matrix, the reinforcements or the matrix/reinforcement interfaces. The choice of the cohesive law parameters assumes that $\sigma_{max} = E/200$ for each constituent with E being the Young's modulus and $\phi_0 = (1-\nu^2)K_{IC}^2/E$ with K_{IC} being the mode-I fracture toughness of the materials in question.

Two different sets of parameters for the Al_2O_3/TiB_2 interfaces are chosen. The first set of cohesive parameters characterizes the ideally bonded interfaces between the two phases (strong interface). This set of parameters assumes the interfaces have the same bonding strength and cohesive energy as the Al_2O_3 matrix ($\overline{T}_{max}^{interface} = \overline{T}_{max}^{matrix}, \phi_0^{interface} = \phi_0^{matrix}$). The second set of parameters represents significantly weakened interfaces along the phase boundaries. Specifically, the maximum traction $\overline{T}_{max}$ and ϕ_0 are 1/10 of those of the alumina matrix ($\overline{T}_{max}^{interface} = 0.1\overline{T}_{max}^{matrix}$, $\phi_0^{interface} = 0.1\phi_0^{matrix}$). Materials outside the crack-tip region are assumed to be homogeneous and are assigned a set of effective parameters representative of those for the Al_2O_3/TiB_2 ceramic composite. Both regions are discretized in the same manner, using both the bulk and the cohesive surface constitutive descriptions. The specimen is stress free and at rest initially. Tensile loading is applied by imposing symmetric velocity boundary conditions along the upper and lower edges of the specimen. For the results discussed here, the imposed boundary velocity is V_0=2 m/s for each edge with a linear ramp from zero to this maximum velocity in the first 0.01 μs of loading. All other specimen surfaces have traction-free boundary conditions.

The cohesive finite element method (CFEM) allows explicit resolution of fracture events as well as permitting the account of arbitrary microstructures. Through the use of the damage parameter D defined in (3), the spatial distribution and time evolution of damage and failure in different microstructures can be compared. This approach not only demonstrates the final outcome of fracture or the fully formed fracture surfaces but also reveals the partially formed fracture patterns or attempted fracture paths.

RESULTS

Two microstructures are considered here. One has the strong bonding and the other has the weak bonding between the phases. Both microstructures have the same TiB_2/Al_2O_3 phase morphologies. Figure 2 shows the distributions of the damage parameter D in these two microstructures. The microstructure in Fig. 2(a) has the strong bonding and the microstructure in Fig. 2(b) has the weak bonding. The plots are for t = 0.13 μs after the beginning of loading. The phase boundaries are outlined by solid lines for visualization of the phase morphologies. The pre-crack is on the left and crack propagation is toward the right. The result in Fig. 2(a) shows the propagation of a main crack from the tip of the pre-crack. The crack primarily goes though the matrix and the phase boundaries, although fracture of TiB_2 is also seen. In contrast, the mode of failure in Fig. 2(b) is the simultaneous formation of microcracks throughout the microstructure. There is not a primary crack path. Due to weakening by the distributed microcracks, the stress levels in the microstructure are lower compared with those in Fig. 2(a). In Fig. 2(a), damage is concentrated along crack surfaces. In addition, lower levels of damage are also seen in regions away from the fully formed crack paths. Severe damage occurs at the tip of the main crack tip. In Fig. 2(b), damage is distributed. The contours clearly indicate that separation occurs primarily along the interphase interfaces. This process can occur independently of the main pre-crack. Coalesced microcracks eventually link up with the pre-crack, resulting in the failure of the material.

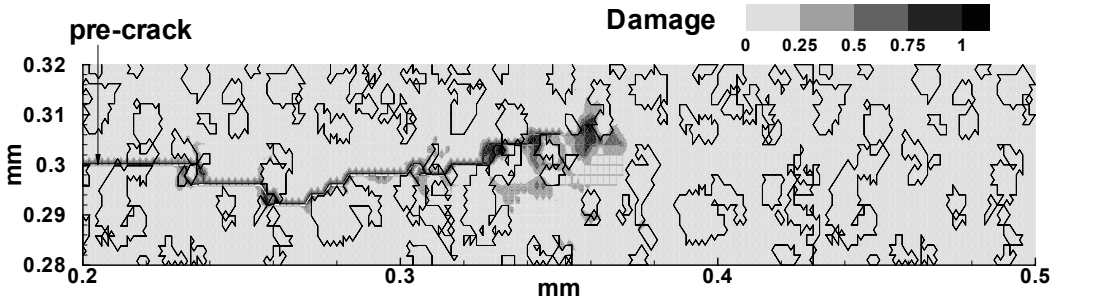

(a)

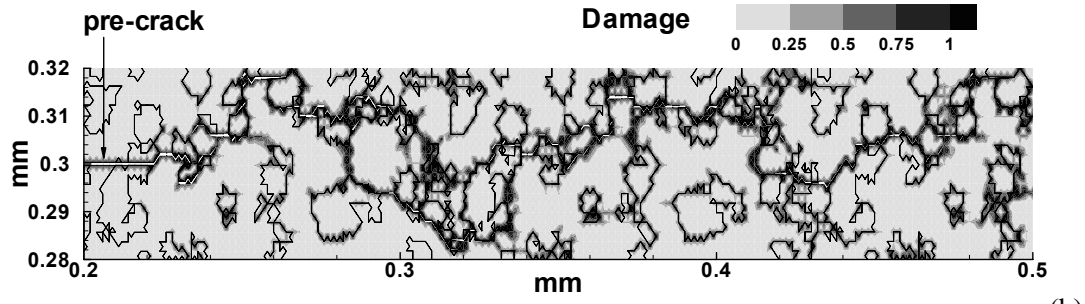

(b)

Fig. 2 A comparison of damage distributions for microstructures with (a) strong interphase bonding and (b) weak interphase bonding

CONCLUSIONS

A micromechanical framework of analysis has been developed and used to provide explicit incorporation of arbitrary material microstructures into numerical modeling and to resolve arbitrary, unconstrained fracture patterns in heterogeneous, brittle solids. The approach combines descriptions of bulk constituent response and fracture surface cohesion. This approach is especially appropriate for analyzing microscopic damage and failure over a range of length scales because material separation is a natural outcome of constitutive behavior, microstructure and loading in this model. The formulation is free from failure criteria valid over only certain length scales, for example, continuum mechanics criteria based on the existence of K-fields.

The interfacial relation allows the energy dissipation during fracture processes to be tracked. When assessed as a fraction of the cohesive energy for the undamaged interfaces, the irreversible energy loss can be used as a measure for damage associated with crack and microcrack development. The damage evolution in an Al_2O_3/TiB_2 composite system is analyzed under the context of a centered-cracked specimen and the

conditions of plane strain. The results demonstrated the effects of interphase bonding on damage and failure development. Calculations show that the failure mode is significantly influenced by the interfacial bonding strength between the phases. When weak interfacial strength exists, microcrack initiation and growth are the principal mode of failure. Whereas when strong interfacial strength is derived from material processing, the advancement of a dominant crack and crack branching are observed. Under the conditions of this analysis, the simultaneous formation of microcrack and their coalescence allow more energy to be dissipated in a material with weak interphase bonding than in a material with strong interphase bonding.

ACKNOWLEDGEMENT

Support from the U.S. Army Research Office through grant DAAG55-98-1-0454 and through NSF CAREER award CMS9984298 is gratefully acknowledged. Calculations are carried out on the Cray Computers at the San Diego Supercomputer Center, Jet Propulsion Laboratory and the Naval Oceanographic Office. We would like to thank Drs. K. V. Logan and N. Thadhani for helpful discussions on ceramic materials.

REFERENCES

Komanduri, R., (1989), Advanced ceramic tool materials for machining, *Int. J. Refract. Hard. Met.*, 8, pp. 125-132.

Messer, P.F., (1991), The Strength of Dental Ceramics, *J. Dent.*, 18, pp.227-235.

Niihara, K., Nakahira, A., and Sekino, T., (1993), New Nanocomposite Structural Ceramics, *Mat. Res. Soc. Sym. Proc.*, 286, pp.405-412.

Logan, K.V., (1992), Shapes Refractory Products and Method of Making the Same, U.S. Patent # 5141900.

Logan, K.V., (1996), Composite ceramics, final technical report, USSTACOM DAAEO7-95-C-R040.

Curran, D.R., Seaman, L., Cooper, T. and Shockey, D.A., (1993), Micromechanical Model for Continuum and Granular Flow of Brittle Materials under High Strain Rate Application to Penetration of Ceramic Targets, *Int. J. Impact Eng.*, 13, pp.53-58.

Rajendran, A.M., (1994), Modeling the Impact Behavior of AD85, Ceramic under Multiaxial Loading, *Int. J. Impact Eng.*, 15, 749-768.

Johnson, G.R. and Holmquist, T.J., (1992), A Computational Constitutive Model for Brittle Materials Subjected to Large Strains, High Rates, and High Pressure, Meyers, M.A., Murr, L.E., and Staudhammer, K.P., editors, Shcock Wave and High Strain Rate Phenomena in Materials, pp.1075-1081.

Espinosa, H. D., Brar, N. S., (1995), Dynamic Failure Mechanisms of Ceramic Bars: Experiments and Numerical Simulations, *J. Mech. Phys. Solids*, 43, pp. 1615-1638.

Zhai, J. and Zhou, M., (1999) Finite Element Analysis of Micromechanical Failure Modes in Heterogeneous Brittle Solids, to appear in *International Journal of Fracture*, special issue on *Failure Mode Transition in Solids*;

Xu, X. -P. and Needleman, A., (1994), Numerical simulations of fast crack growth in brittle solids, *J. Mech. Phys. Solids*, 42, pp.1397-1434.

Zhai, J. and Zhou, M., (1998) Micromechanical Modeling of Dynamic Crack Growth in Ceramic Composites, *Mixed Mode Crack Behavior*, ASTM STP 1359, K. Miller and D. L. McDowell, eds., 1998;